

Ulrich H. Faul · Dean Scott

Grain growth in partially molten olivine aggregates

Received: 11 April 2005 / Accepted: 25 October 2005 / Published online: 6 December 2005
© Springer-Verlag 2005

Abstract Grain growth rates in partially molten olivine aggregates were determined experimentally at a pressure of 1 GPa. The aim of the experiments with fine-grained starting material (solution–gelation derived $F_{O_{90}}$ olivine with a grain size of $\sim 1 \mu\text{m}$ with 2 and 4 wt.% added basaltic glass) was to determine growth rates during steady-state grain growth. A series of experiments was conducted at a fixed temperature of 1,350°C for durations from 2 to 700 h, and a second series at fixed duration (168 h) at temperatures from 1,250 to 1,450°C. The resulting activation energy ($E = 390 \text{ kJ/mol}$) and growth exponent ($n = 4.3$) are comparable to melt-free results (Nichols and Mackwell 1991). The observed grain size distributions are broader than those predicted for normal grain growth or Ostwald ripening and most similar to the Log-normal distribution. The observed melt distribution is influenced by the continuous rearrangement of neighboring grains during growth. The relatively large growth exponent observed in this study and by Nichols and Mackwell (1991) where secondary phases are present suggests that grain growth in the upper mantle is slower than predicted by Karato (1989).

Keywords Grain growth · Olivine · Partially molten rocks

Introduction

The size of the crystalline grains in the Earth's upper mantle affects a number of physical properties, for example deformation (Hirth and Kohlstedt 1995), seismic velocities and attenuation (Faul and Jackson 2005),

electrical conductivity (ten Grotenhuis et al. 2004) and permeability of partially molten rocks (Faul 2001). The grain growth rate relative to deformation influences the dynamical behavior of the mantle (Solomatov 2001). While grain growth experiments have been conducted with melt-free olivine (Karato 1989; Nichols and Mackwell 1991), comparable data for melt bearing olivine is not available.

Previous studies of grain growth kinetics in melt-free olivine involved crushed natural olivine aggregates either at moderate pressure (300 MPa) but relatively short duration (less than 24 h) (Karato 1989), or at 1 atm for up to 200 h (Karato 1989; Nichols and Mackwell 1991). Karato (1989) found that the presence of pores significantly inhibits grain growth while water enhances it. He concluded that where pores or second phase particles are unimportant, grain growth in olivine is fast relative to geologic time scales. Nichols and Mackwell (1991) investigated the oxygen fugacity dependence of grain growth. They found that growth rates increase with increasing oxygen fugacity, but that in their 1 atm experiments growth was controlled by coalescence of pores, with growth rates limited by diffusion of the slowest ionic species constituting olivine.

The experiments described here are designed to investigate grain growth in partially molten olivine aggregates at low melt fractions. The use of a piston cylinder apparatus allowed the experiments to be conducted at relatively high pressure to avoid pores, and long durations (up to 700 h) to determine steady-state growth rates. The latter was achieved by using a very fine-grained, fully synthetic starting material. With this fine-grained starting material the samples should evolve relatively quickly to a grain size distribution which, when normalized by the mean grain size, is time invariant (or self-similar). The grain growth kinetics derived from these experiments therefore are independent of the initial grain size distribution and refer to steady-state grain growth, which is presumably similar to grain growth at the much longer time scales in the Earth.

Communicated by T.L. Grove

U. H. Faul (✉) · D. Scott
Research School of Earth Sciences, The Australian National
University, Canberra, ACT 0200, Australia
E-mail: uli.faul@anu.edu.au
Fax: +61-2-61258846

Theoretical

Normal grain growth and Ostwald ripening

The type of grain growth investigated here is that driven by a reduction of grain boundary energy (a decrease of the surface to volume ratio), generally described as normal grain growth or Ostwald ripening (see e.g., Evans et al. (2001) for a review of other growth/recrystallization mechanisms). In both processes the driving force is the reduction in Gibbs free energy due to the decrease in grain surface area with increasing mean grain size. The driving force or potential D is related to the grain size r :

$$D \propto \frac{\gamma}{r} \quad (1)$$

where γ is the surface energy.

Theoretical treatments of normal grain growth start by describing the decrease in internal pressure with increasing radius (Atkinson 1988), while theoretical treatments of Ostwald ripening are based on the higher solubility (increased chemical potential) of smaller particles relative to larger particles embedded in a matrix with a mean concentration (mean field theories) (Lifshitz and Slyozov 1961; Wagner 1961). For normal grain growth the volume fraction of the growing phase does not enter into the derivation, while for Ostwald ripening “infinite” dilution of the growing phase is assumed.

Normal grain growth is usually used to describe the coarsening of single phase systems (e.g., pure metals), while the growth of dispersed grains in a solid or liquid matrix is usually described by Ostwald ripening (e.g., growth of garnet in metamorphic rocks).

Both theories predict simultaneous growth and shrinkage of individual crystals in an aggregate, where in a closed system the total number of crystals decreases while their mean radius increases. Both types of grain growth predict a relatively narrow range of shapes and grain sizes and the time invariance of the normalized grain size distribution (Atkinson 1988). This contrasts for example with a broader grain size distribution due to so-called primary grain growth, driven by annealing of high dislocation densities after deformation, or dynamic recrystallization during deformation. Since the driving force for normal grain growth/Ostwald ripening is always present in the Earth (as long as it is not a single crystal) this growth process is always operating and competes with grain size reduction due to deformation (Karato 1989).

For both Ostwald ripening and normal grain growth a growth equation of the form:

$$r^n - r_0^n = kt \quad (2)$$

can be derived, where r_0 is the grain size at the start of the experiment, r the grain size at time t , k a rate constant and n a growth exponent. The temperature dependence of the rate constant is expressed as:

$$k = k_0 e^{-E/RT}, \quad (3)$$

where E is the activation energy and k_0 is a characteristic constant for a particular growth process and environment.

For normal grain growth of pure, single phase systems a growth exponent of $n=2$ is derived, while $n>2$ has been predicted for various control mechanisms in systems with secondary phases present. However, identification of the controlling mechanism is often difficult (Atkinson 1988).

During Ostwald ripening potentially growth rate limiting steps are detachment of growth units from the surface of a shrinking crystal, their diffusion through the matrix, and reattachment to a growing crystal. Two principal cases can therefore be distinguished: diffusion controlled growth and interface reaction controlled growth (Martin et al. 1997). For diffusion controlled growth the concentration gradient between particles depends on particle spacing or volume fraction (Fischmeister and Grimvall 1975). If the rate of attachment to the crystal surface is the rate limiting step, the kinetics become identical with those for Ostwald ripening of a distribution of second phase particles (Atkinson 1988, p. 474). For diffusion controlled growth $n=3$ is predicted, while for interface reaction controlled growth the predicted exponent is $n=2$ (Wagner 1961).

Grain size distributions

Since the normalized grain size distributions predicted for steady-state growth are time-invariant, the distributions are potentially diagnostic as to whether steady state has been reached in an experiment or in natural rocks, or whether other processes (e.g., deformation) affect grain growth.

Grain size distributions predicted for both normal grain growth and diffusion controlled Ostwald ripening are narrow (the largest grain size is smaller than $2\times$ the mean grain size, r_{mean}) and have the peak of the distribution at or above the mean grain size (Lifshitz and Slyozov 1961; Hillert 1965).

Hanitzsch and Kalhweit (1969) have calculated grain size distributions for Ostwald ripening of cylindrical particles (Fig. 1). The diffusion controlled case shows the typical narrow distribution with a relatively sharp cutoff of the distribution towards larger grain sizes at $1.5\times r_{\text{mean}}$. The distribution has its maximum above the mean grain size. In contrast, the distribution predicted for second order surface reactions, where growth occurs layer by layer spreading on faceted crystal surfaces (e.g., Bennema and van der Eerden 1987), has a tail of the distribution to a radius $r\sim 2.5\times r_{\text{mean}}$. The maximum of the distribution is below r_{mean} .

Also shown in Fig. 1 are the Rayleigh distribution derived on the basis that the motion of grain boundaries during growth is random (Louat 1974; see also German and Olevsky 1998), and the Log-normal distribution.

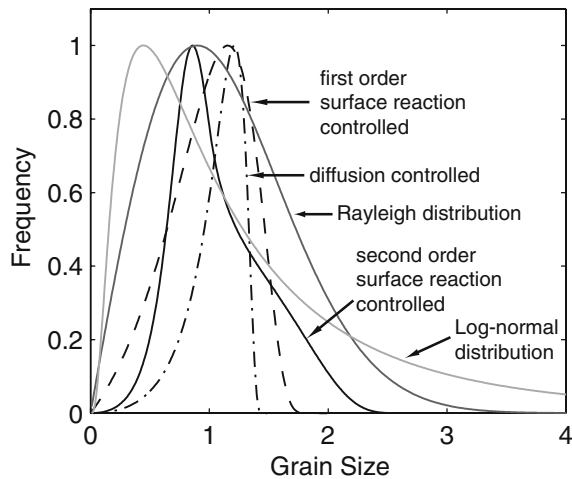


Fig. 1 Normalized grain size distributions predicted for Ostwald ripening of cylindrical particles Hanitzsch and Kalhweit (1969), as well as the Rayleigh distribution (Louat 1974) and the Log-normal distribution. The distribution predicted for diffusion controlled Ostwald ripening is narrow and has its maximum above the mean grain size with a sharp cut-off to larger sizes. The distribution predicted for second order surface reaction controlled growth has its maximum below the mean grain size and a longer tail to larger grain sizes. The Rayleigh distribution has a similar maximum, but is wider with a longer tail to larger grain sizes. The Log-normal distribution is more strongly skewed towards small grain sizes with a long tail to large sizes

The Log-normal distribution is, however, not based on a rigorous solution of the grain growth equations (Atkinson 1988). The Rayleigh distribution is given by:

$$f_R = \frac{x e^{(-x^2/2\sigma^2)}}{\sigma^2}, \quad (4)$$

where σ determines the width of the distribution. The Log-normal distribution is given by:

$$f_L = \frac{1}{x\sigma\sqrt{2\pi}} e^{-(\ln x - \mu)^2/2\sigma^2}, \quad (5)$$

where μ is the log of the mean of the distribution and σ is again treated as an adjustable parameter influencing the shape of the distribution.

Experimental

Grain size and melt distribution from starting materials with an average grain size $>10\text{--}20\ \mu\text{m}$ indicate that hundreds of hours at high temperatures are necessary to reach the steady-state grain growth process described above (Faul 1997). A uniformly fine-grained starting material is therefore obtained by a solution–gelation method. A brief description of this method is given in the following paragraph (see also Jackson et al. (2002)).

Magnesium nitrate and ferric nitrate in the proportions required for an olivine composition of $\text{Mg}_{1.8}\text{Fe}_{0.2}\text{SiO}_4$ are dissolved in ethanol after calibrating the actual metal-oxide content of the nitrates. Silica is

added in the form of tetra-ethyl orthosilicate (TEOS). The mixture is continuously stirred with a magnetic stirrer. A few drops of nitric acid initiate the gelation process on a hot plate at $\sim 30^\circ\text{C}$.

The gel is progressively dried at increasing temperatures (initially in a fume-hood) with the final step at $1,050^\circ\text{C}$ for 1 h in air. The dried gel is ground and pelletized. The pellets are then run for >12 h in a controlled oxygen atmosphere furnace suspended in a Pt-wire cage. The oxygen fugacity is set by a 50% CO/50% CO_2 gas mixture at a temperature of $1,400^\circ\text{C}$ ($f_{\text{O}_2} \sim 10^{-8} - 10^{-9}$ atm). The resulting plugs are highly porous. SEM observations indicate that the olivine grain size after reaction is well below $1\ \mu\text{m}$.

To obtain melt at high temperatures, sintered oxide derived basaltic glass powder is gently ground together with the sol–gel derived olivine in an agate mortar. The composition of the added basaltic glass is given in Table 2 of Faul et al. (2004). The amount of melt shown in Table 1 is the weight percent of basaltic glass added to the olivine. The basalt composition is designed to be approximately in equilibrium with a four phase assemblage (olivine, two pyroxenes and plagioclase) at 300 MPa and $\sim 1,250^\circ\text{C}$ (Cmíral et al. 1998). Quantification of the melt (glass) and orthopyroxene (opx) proportions at $1,300^\circ\text{C}$ in an experiment at 300 MPa with 4 wt.% glass added gives a melt content of 3.7% at run conditions and an opx content of nearly 1% (Faul et al. 2004). At $1,250^\circ\text{C}$ slightly more opx is present, whereas at $1,450^\circ\text{C}$ almost no opx is left. The melt content varies accordingly, although there may also be minor changes in the olivine proportion.

All runs were carried out in a 1.27 cm diameter piston cylinder apparatus at a pressure of 1 GPa. Table 1 gives a list of run conditions and mean grain sizes. The furnace assembly was chosen to be anhydrous and consists of an outer NaCl sleeve, Pyrex glass, graphite heater and inner spacers of MgO. The outer Pt capsule is separated from the graphite heater by a thin MgO sleeve. The inner capsule in contact with the sample is made from high purity graphite. All furnace components were oven-dried at $\sim 200^\circ\text{C}$.

Temperature and run duration are controlled by a Eurotherm controller using a type B (Pt–Rh) thermocouple. Power is stepped to zero after a preset time, resulting in initial quench rates $>100^\circ\text{C/s}$. To avoid melt segregation due to thermal gradients (Leshner and Walker 1988) the sample is placed at the center of the hot zone of the furnace. The temperature at the thermocouple is corrected for the resulting offset by calibration using differential thermal analysis with the melting point of gold. Relative temperature uncertainties of this study are estimated to be $<10^\circ\text{C}$, absolute uncertainties may be somewhat larger.

The oxygen fugacity (f_{O_2}) is not buffered, but the presence of graphite limits f_{O_2} to below the graphite–C–O vapor buffer (Taylor and Green 1989; Ulmer and Luth 1991). The silica activity is buffered by the presence of orthopyroxene, which originates from an amount of

Table 1 Experimental data and grain size distribution fit parameters

Experiment (wt.% basalt)	Time hours	Temp., °C	Mean grain size, μm	Standard deviation ^a	Maximum grain size ^a	χ^2 Log-normal ^b	χ^2 Rayleigh ^c	Number of grains
sgob7 (2)	2	1,350	9.2	0.66	4.3	30	101	420
sgob1 (2)	24	1,350	14.5	0.75	4.7	56	376	608
sgob2 (2)	170	1,350	25.8	0.64	3.3	25	84	556
sgob8 (2)	432	1,350	33.2	0.58	3.8	42	47	479
sgob3 (2)	700	1,350	31.0	0.69	3.9	21	120	390
sgob9 (2)	168	1,250	17.3	0.68	4.6	23	112	511
sgob4 (2)	168	1,300	17.9	0.75	4.4	28	153	283
sgob5 (2)	168	1,400	28.2	0.67	5.7	34	98	486
sgob6 (2)	168	1,450	38.4	0.63	3.4	20	46	264
sgob13 (4)	2	1,350	8.5	0.63	5.6	64	104	596
sgob10 (4)	168	1,350	27.0	0.54	3.0	65	36	418
sgob11 (4)	432	1,350	33.4	0.53	2.8	48	26	250
sgob12 (4)	168	1,250	16.3	0.64	3.0	35	116	542
OB2 ^d (2.5)	313	1,300	37.0	0.80	5.9	34	199	212

^aNormalized by the mean grain size

^b χ^2 value calculated for normalized grain size distribution with a binwidth of 0.2 ($\sim 0.3 \times$ standard deviation). The number of bins is set such that no bin of the predicted distributions has a value < 1 and no more than $1/5$ th of the total number of bins have a value < 5 for the experiment with the smallest number of grains measured (sgob6). For 16 bins, resulting in 14 degrees of freedom (σ in Eqs. 4 and 5 for both distributions has been chosen to optimize the fit, reducing the degrees of freedom by one), the χ^2 value for rejection of the hypothesis that the experimentally observed and predicted distributions are the same with $p = 0.05$ is 23.7. (See for example <http://helios.bto.ed.ac.uk/bto/statistics/tress9.html>, <http://www.itl.nist.gov/div898/handbook/eda/section3/eda35f.htm>)

^cDue to the smaller number of grains in the tail to large grain sizes of this distribution the number of bins is reduced to 15, with the same bin width as for the Log-normal distribution. For $p = 0.05$ $\chi^2 = 22.4$

^dFrom Faul (1997)

silica added to the gel, which is slightly in excess of the stoichiometrically required amount for olivine. Olivine in the melt added aggregates is of composition Fo_{90} and contains $1,270 \pm 40$ wt. ppm Ca (0.18 wt% CaO) and 370 ± 130 wt. ppm Al (0.07 wt% Al_2O_3). No inhomogeneity of the melt distribution at the sample scale is observable even in experiments of only 2 h duration (Fig. 2).

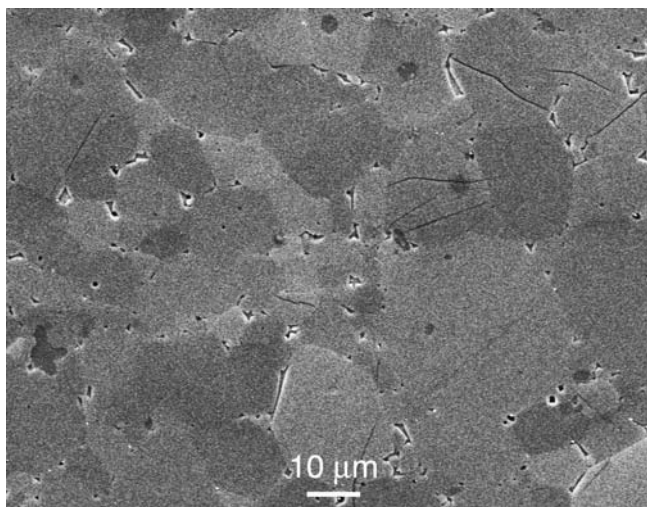


Fig. 2 Backscattered electron (BSE) image of run sgob7 with 2 wt.% melt added, a run duration of 2 h at 1,350°C, and a mean grain size of 9.2 μm . The relatively large increase in grain size from a starting grain size of ~ 1 μm ensures that the melt is homogeneously distributed even after a short run duration

After the experimental run each sample was sectioned vertically through the center, mounted in epoxy and polished with diamond, then alumina and finally with colloidal silica to obtain an undamaged surface for imaging. Grain sizes were determined by tracing grain boundaries on screen from digital backscattered electron (BSE) images (Figs. 2, 3). The location of a grain boundary was inferred by connecting the cusps of adjacent melt pockets, aided by orientation contrast where visible.

The grain size is calculated from the circle-equivalent area of each grain in an image and multiplied by $4/\pi$ to correct for sectioning effects of a sphere. For the digital image processing and feature analysis the public domain software NIH Image was used. To check the accuracy and reproducibility of the so determined grain sizes two samples (sgob2 and sgob7) were subsequently also mapped by electron backscatter diffraction (EBSD) (Fig. 4) in an SEM with W-filament using the HKL EBSD software package. The resulting mean grain sizes are within 4% of the manually obtained ones. This figure also indicates the magnitude of the relative error in the grain size determinations of each run.

Results

Growth parameters

The experiments were designed to constrain grain growth kinetics with runs at a fixed temperature (1,350°C) and increasing duration (from 2 to 700 h), and

Fig. 3 Backscattered electron (BSE) image of run sgob11 (432 h at 1,350°C, 4 wt.% melt added). Olivine grains show some orientation contrast after polish with colloidal silica. Melt (quenched to glass) is *lightest*, orthopyroxene grains are *darkest*, cracks due to quench are *black*. Faceting of olivine–melt interfaces is evident. *Numbers* indicate the figures with high-resolution images of these melt pockets. Note the size of the triple junctions in Fig. 6a, b relative to the large melt pockets. Idealized models (e.g., reticulite, Wark et al. 2003, their Fig. 11) do not show this variation in the size of melt pockets. Opx denotes an orthopyroxene grain, *gr* graphite

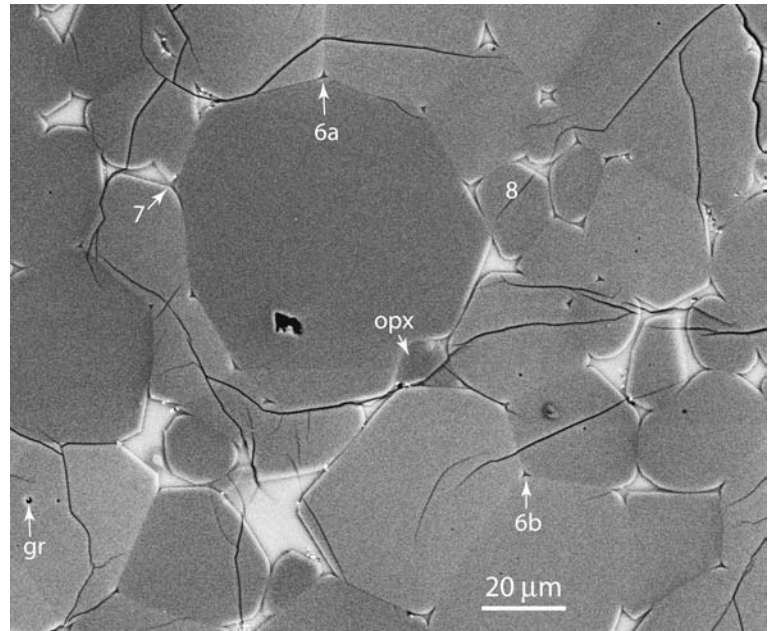
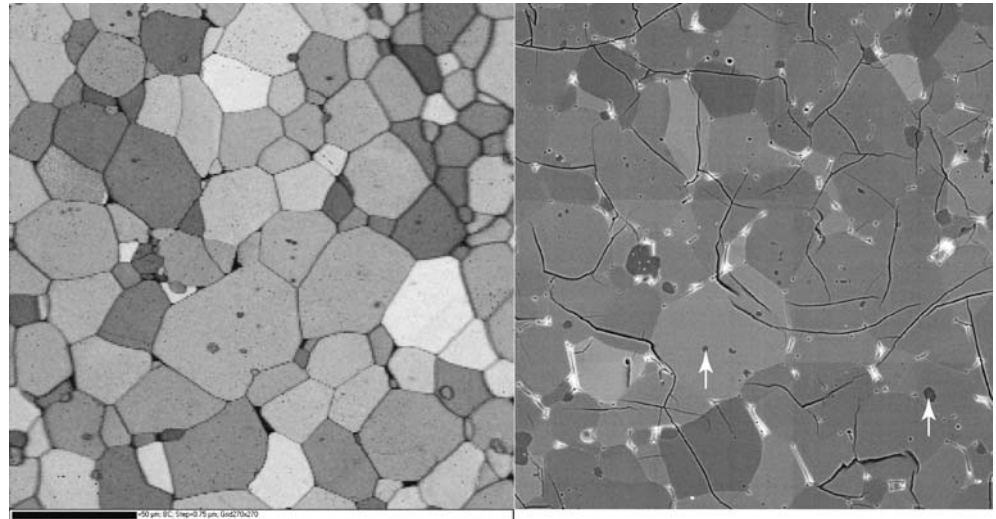


Fig. 4 Images of run sgob2 (170 h at 1,350°C). *Left* band contrast image from EBSD mapping. Grain boundaries and larger melt pockets are dark due to their low or absent band contrast. While olivine–melt interfaces are often faceted, olivine–olivine boundaries are more commonly slightly curved. *Right* BSE image of the same area. A comparison of the images shows that EBSD mapping at this scale (step size 0.75 μm) only resolves larger melt pockets. Two opx grains included in olivine are indicated by *arrows*. The *black scale bar* at the bottom left indicates 50 μm



activation energy with runs at fixed duration (168 h) at a range of temperatures (1,250–1,450°C). The results are shown in Fig. 5 in a plot of run duration versus grain size. No abnormal grain growth (where a few grain grow much faster than the majority of grains) was observed in any of the experiments. Four repeat experiments were conducted where the amount of basalt powder added before the experiment was doubled (to 4 wt.%, Table 1). The resulting grain sizes are within error of the grain sizes of the experiments with 2 wt.% melt added. Also shown in Fig. 5 is an estimated 10% cumulative error in the grain size due to uncertainties in temperature and grain size measurements.

The grain growth exponent n , constant k_0 and activation energy E are determined by a non-linear least-squares fit of the experimental data in Table 1 (except for OB2) to Eqs. 2 and 3. The resulting best-fit parameters

are: $k_0 = 8.2 \times 10^{-14} \text{ m}^n \text{ s}^{-1}$, $E = 390 \text{ kJ/mol}$ and $n = 4.3$ for a starting grain size $r_0 = 1 \text{ μm}$. The longest experiment (sgob3, 700 h) has the largest residual error. The standard deviation from the fit to the 13 experiments is $\sigma = \sqrt{\sum (r_{\text{calc}} - r_{\text{meas}})^2 / (n - 1)} = 1.95 \text{ μm}$.

Melt distribution

In images of sample sections, melt (now quenched to glass) occurs at all three-grain edge intersections, forming a completely interconnected network of melt in three dimensions (Figs. 2, 3, 6, 7, 8). Examination of three-grain edges from similar experiments by transmission electron microscope (TEM) shows that this triple junction network is present at melt contents as low as 0.01 vol.% (Faul et al. 2004). While some triple junction

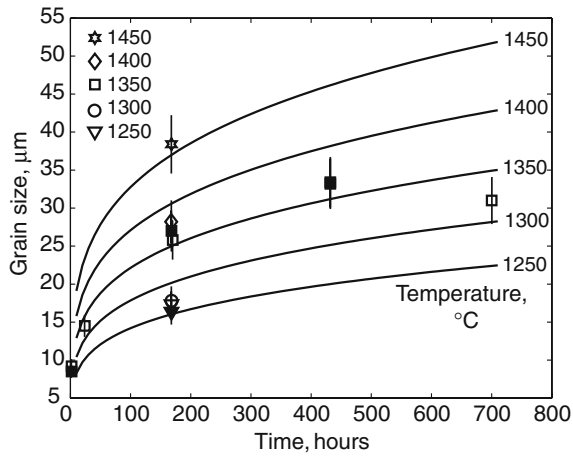


Fig. 5 Grain growth data (*open symbols*: 2 wt.% basalt added, *closed symbols* 4 wt.% basalt added) and non-linear least squares fit to the data (Table I, except OB2). The two runs at 1,350°C and 432 h have nearly identical grain sizes. The *error bars* indicate a cumulative error of 10% from uncertainties in temperature and grain size determination

tubules have geometries that closely resemble those predicted by idealized models (e.g., Fig. 6b) (von Bargen and Waff 1986; Wark et al. 2003), most are affected by faceting of at least one of the olivine crystals involved (Figs. 3, 6, 7, 8). In the more coarse-grained samples the triple junction tubules (melt pockets surrounded by no more than three grains) are generally small, and most of the melt resides in pockets surrounded by four or more grains (Fig. 3). These larger melt pockets also often involve faceted crystal–melt interfaces.

In order to adequately resolve the melt geometry high resolution imaging is necessary. While not obvious at lower magnification, melt frequently penetrates deep between two-grain boundaries (compare Fig. 3 with Figs. 6, 7, 8), in some cases connecting to neighboring melt pockets with uniform thickness (Fig. 6a). Quench growth is only observable at the transition from faceted to rounded olivine–melt interfaces (Fig. 8).

Dihedral angles measured at low magnification consequently often overestimate the actual dihedral angles. Thirty-two dihedral angles measured with NIH Image from ten high-resolution images from the area covered by Fig. 3 have a median of 12°, a value that is somewhat larger than that determined by TEM imaging [$\leq 10^\circ$ (Cmíral et al. 1998)]. Two angles in this area have a value of zero where the melt connects to a neighboring melt pocket with a width < 100 nm.

Walte et al. (2003) show in directly observable grain growth experiments with analogue materials that fully or partially wetted two-grain boundaries and melt pockets surrounded by more than three grains are formed when smaller grains shrink and disappear and the surrounding grains need to adjust their shape to fill the space. Similarly, the range of melt geometries observed in partially molten olivine aggregates during grain growth are influenced by continuously changing arrangements of

neighboring grains. One difference to the analogue materials of Walte et al. (2003) is the faceting of olivine–melt interfaces. This tendency to develop facets may lead to the stabilization of relatively large melt pockets at larger mean grain sizes (Fig. 3).

Partially molten rock undergoing grain growth will therefore have a melt distribution that differs from that predicted by static models with uniform grain size and fixed dihedral angle (von Bargen and Waff 1986; Wark et al. 2003). This difference in geometry may have significant consequences for example for permeability (Faul 2001). It may explain at least qualitatively the difference between the permeability predicted for idealized systems (von Bargen and Waff 1986) and the permeability measured with analogue materials (Wark and Watson 1998; Wark et al. 2003).

Grain size distributions

During grain growth the grain size distributions broaden with increasing mean grain size. The maximum grain size increases from 40 μm after 2 h at 1,350°C to 120 μm after 700 h. It is therefore easier to compare grain size distributions that are normalized by their mean grain size. These normalized distributions should also be time invariant during steady-state growth. Examples of normalized grain size distributions are shown in Fig. 9.

In order to assess the time invariance, a χ^2 test was used to compare the grain size distributions observed in the experiments to the grain size distributions shown in Fig. 1 and given in Eqs. 4 and 5. The parameter σ in these equations was chosen to minimize the calculated χ^2 values ($\sigma = 0.9$ for both the Rayleigh and Log-normal distribution). The χ^2 values shown in Table 1 indicate that the observed distributions of the runs with 2 wt.% melt added have the smallest misfit relative to a Log-normal distribution, but are in most cases not identical with this distribution.

The calculated χ^2 values do not systematically change with increasing temperature or experimental duration. This suggests that the distributions are largely time invariant as required for steady-state grain growth. A caveat is that due to the small number of grains in the long tails to large grain sizes, the grains in the tails of each of the distributions have to be combined into one bin to satisfy the requirements of the χ^2 test. The observed decrease in the maximum grain size with increasing time and temperature (Table 1) suggests that the distributions actually become somewhat narrower.

The calculated χ^2 values depend somewhat on the number of bins used. Increasing the number of bins in the χ^2 test where this is possible due to the larger number of grains measured generally increases the calculated χ^2 value for the Log-normal distribution, while the value for the Rayleigh distribution decreases. This reflects the larger number of grains expected in the tail of the Log-normal distribution relative to the observations (Fig. 9). The Rayleigh distribution tends to provide a better fit to

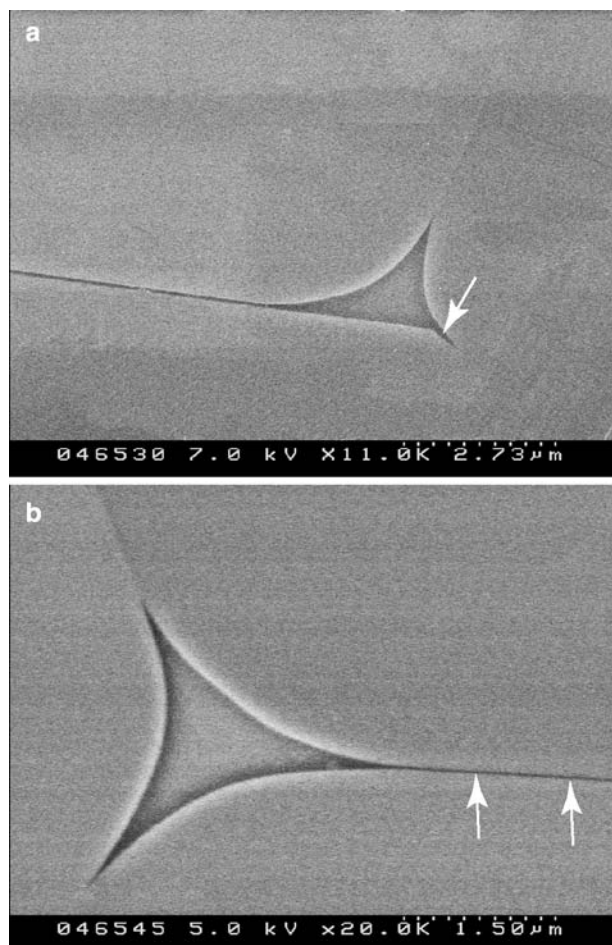


Fig. 6 Field emission scanning electron microscope (FESEM) and secondary electron (SE) images showing detail from Fig. 3. **a** The apparently wetted grain boundary (with a constant width of the melt layer) can be followed over a distance of more than 20 μm to the adjacent melt pocket. Note also the small dihedral angle due to faceting on the right of the triple junction (*arrow*). **b** Melt penetrates deep between two grain boundaries (*arrowed*) but becomes too thin a few micrometers from the next triple junction to be resolved by FESEM imaging. The dihedral angle is very small

the distributions observed at longer run durations at 1,350°C and above (Fig. 9b).

The distributions of the runs with 4 wt.% melt added are narrower than the distributions with the smaller melt fraction (except the shortest run) (Fig. 9c). They therefore tend to have a smaller misfit relative to the Rayleigh distribution, although again they do not coincide with this distribution (Table 1).

Of the distributions calculated for Ostwald ripening by Hanitzsch and Kalhweit (1969) the distribution predicted for diffusion controlled growth is far too narrow and has the peak in the wrong position relative to the experimental distributions. The distribution for second order surface reaction controlled growth is the most similar to the experimental distributions, although the χ^2 values are much larger than for the Log-normal and Rayleigh distributions.

An experiment with a much larger starting grain size range (45–62 μm) still has a relatively large χ^2 value even after more than 300 h at 1,300°C. Small starting grain sizes are therefore necessary if a steady-state grain size distribution is desired in an experiment.

Discussion

Secondary phases and inclusions

As indicated in the [Experimental](#) section, a minor amount of opx is present in the samples (Figs. 2, 3, 4). Figure 3 shows most clearly that opx grains can exert a drag force on moving olivine grain boundaries. Figure 4 shows much smaller opx grains as inclusions inside olivine grains while a few larger grains remain on olivine–olivine grain boundaries. The size difference between opx grains included in olivine and those on grain boundaries indicates that the opx grains themselves grow as long as they are on grain boundaries.

Overall only a small number of olivine grain boundaries are affected by drag from opx grains. For example, only ~ 1 in 50 two-grain boundaries in Fig. 3 are affected by the presence of opx, although this ratio might be larger at lower temperatures where a slightly larger amount of opx is present. The deviations of the measured grain sizes from the fit show no systematic behavior with temperature as would be expected if the variations in opx content influenced the growth rate.

Transmission electron microscope observations on similarly prepared samples indicate that some of the black spots that can be seen in SEM images (e.g., Fig. 3) are graphite grains, most likely introduced during loading of the graphite capsule. They will presumably also exert a drag force on grain boundaries. However, due to their small size most of the graphite grains become incorporated into olivine grains early on during growth.

How effectively small secondary particles become included into the growing olivine grains may depend in addition to their size also on whether they are located on two-grain boundaries (disconnected from the fast diffusivities of the interconnected melt) or three or more grain edges. The small number of remaining secondary (solid) particles outside of olivine grains suggests that it is unlikely that they influence growth kinetics significantly. Gas-filled pores are essentially absent in melt-bearing samples at a pressure of 1 GPa in this study.

No melt inclusions inside olivine grains are observed in any of the samples, indicating that growth took place in the “pore drag” regime of Renner et al. (2002). The mobility of the grain boundaries even at the highest temperature was never high enough to “drop” pockets of melt, which would lead to the formation of melt inclusions. This is again consistent with the tendency of olivine–melt interfaces to develop slow-growing facets. The grain boundaries were mobile enough, however, to

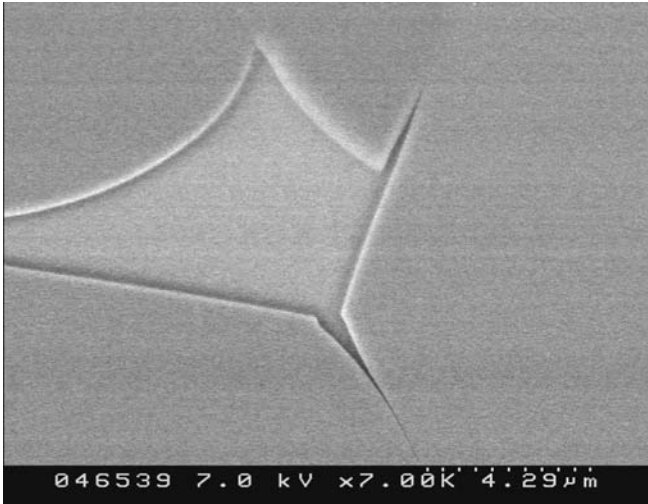


Fig. 7 FESEM-SE image with detail from Fig. 3 showing two dihedral angles which would appear much larger at low magnification due to the faceting of the interfaces. The angle in the lower right corner is again just above zero as in Fig. 6b. The angle at the top left is the largest angle measured in these images. During polishing the softer glass (relative to the olivine crystals) is preferentially removed, creating some topography at olivine-glass edges. This topography causes the bright edges of olivine and the adjacent dark “shadows” in the glass pockets in both BSE and SE images

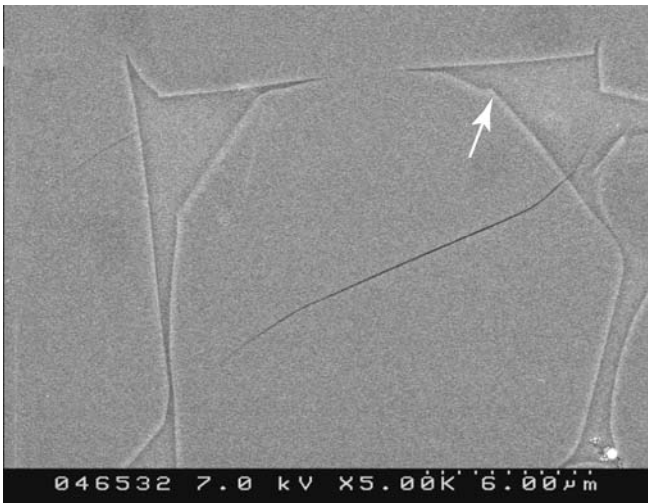


Fig. 8 FESEM-SE image with detail from Fig. 3 showing more clearly the extent of faceting of crystal-melt interfaces. Small irregularities at the transition from faceted to non-faceted interfaces (arrow), observable in many of the images, are likely due to quench growth. Note the size of the dihedral angles

“drop” small opx and graphite grains now found as inclusions inside olivine grains.

Growth mechanism

In the experiments of this study the observed growth exponent ($n \sim 4$) is different to the growth exponents

predicted for Ostwald ripening ($n=2$ for interface controlled growth and $n=3$ for diffusion controlled growth) and normal grain growth of a single phase ($n=2$). The observed grain size distributions do not closely match any of the theoretically predicted distributions, although they are the most similar to the distribution predicted for second order surface reaction controlled Ostwald ripening (Hanitzsch and Kahlweit 1969). Faceting of crystal-melt interfaces also indicates that growth is limited by surface reactions (growth by layer spreading) (Ben-nema and van der Eerden 1987; Waff and Faul 1992).

The combination of these observations suggests that none of the theoretical models takes all the factors into account that contribute to the observed growth behavior. This also implies that the activation energy cannot easily be interpreted in terms of a single controlling growth mechanism such as volume or grain boundary diffusion, as is usually assumed (Ralph et al. 1992).

There are, however, extensions of the basic models that capture aspects of the observed behavior. The width of experimentally observed grain size distributions in other systems frequently exceeds model predictions, and a number of reasons have been cited for this discrepancy. A key assumption for (diffusion controlled) Ostwald ripening is the “infinite dilution” of the growing phase so that each crystal has the same environment (mean-field approximation). In practice this assumption may only be approached for the ripening of widely dispersed secondary phases. Numerical simulations of Ostwald ripening with increasing volume fraction of the ripening phase predict a broadening of the grain size distribution (Tikare and Cawley 1998). Similarly Mulheran (1992) in a model with relaxed mean-field approximation predicts a broader grain size distribution that has a peak at smaller grain sizes (at $0.5 \times r_{\text{mean}}$). Renner et al. (2002) also discuss a broadening of grain size distribution with increasing volume fraction of the ripening phase. The distributions observed by them for grain growth in calcite are similarly skewed to small grain sizes as the distributions observed in this study.

A problem for both Ostwald ripening of a high volume fraction phase as well as normal grain growth of a single phase is that topological constraints for space filling also influence the growth environment (Pande 1987). The presence of melt in partially molten rocks may relax this space filling requirement relative to subsolidus conditions, as the melt conforms to arbitrary shapes. While models for normal grain growth in the presence of secondary phases have been developed, no formal criterion for the transition from Ostwald ripening to normal grain growth with decreasing melt fraction exists (see also Renner et al. 2002). Models for normal grain growth in the presence of secondary phases predict an exponent $n=4$ for cases where growth is controlled by surface diffusion (with pores present) or grain boundary diffusion (Atkinson 1988).

Cabane et al. (2001) in grain growth experiments with quartz plus silicic melt similarly find a growth exponent $n > 2$ suggesting diffusion control, but also observed

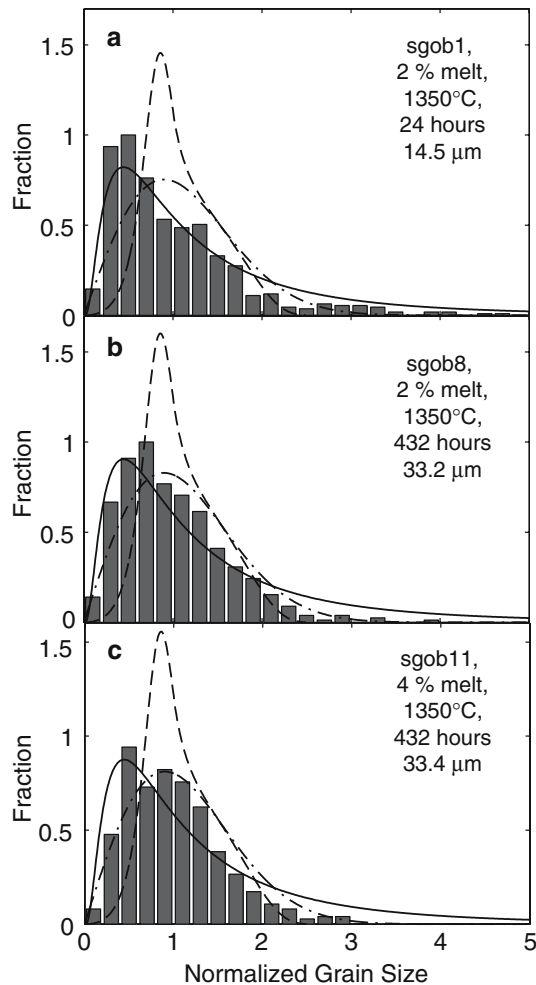


Fig. 9 Histograms of grain size distributions illustrating the tendency for the distributions to become narrower with time and increasing melt content. Experimental distributions with a long tail (a) are better fit by a Log-normal distribution, the more narrow distributions (c) are better fit by a Rayleigh distribution. The grain size is normalized by the mean; the *histograms* by the maximum of the distribution. *Curves* show the distribution predicted for second order surface reaction controlled growth (*dashed*), the Rayleigh distribution (*dash-dotted*) and the Log-normal distribution (*solid*). These calculated distributions are normalized to the same number of grains as each of the experiments shown

faceted quartz–melt interfaces indicative of surface reaction control. They argue that for this system the kinetics are determined by surface reaction-controlled Ostwald ripening of quartz despite the larger than predicted exponent.

Comparison with other studies

Three other studies have investigated grain growth in olivine aggregates at hydrostatic conditions. Karato (1989) determined grain growth rates both at one atmosphere and “wet” and “dry” at 300 MPa. Nichols and Mackwell (1991) determined grain growth rates at one atmosphere as a function of oxygen fugacity. Park

and Hanson (1999) determined grain growth rates of Fo_{100} crystals suspended in a haplobasaltic melt at 1 atm and 1,275°C (< 50% crystalline). Karato’s (1989) 1 atm and the “dry” 300 MPa data, Park and Hanson’s (1999), as well as Nichols and Mackwell’s (1991) data with an oxygen fugacity of 10^{-7} atm along with the fit to the data from this study are shown in Fig. 10.

Grain growth at one atmosphere is assumed to be controlled by the evolution of pores (Karato 1989; Nichols and Mackwell 1991), involving surface diffusion. Similarly at water-saturated conditions grain growth is affected by the presence of pores (Karato 1989). Nichols and Mackwell (1991) found activation energies and growth exponents similar to this study, while Karato’s (1989) 1 atm data indicates a high activation energy and an exponent with a value between 2 and 3. This high activation energy is partly due to the 1,400°C data (see Fig. 10) which is inconsistent with Nichols and Mackwell’s (1991) data as noted by them.

While grain growth of melt-free but porous olivine aggregates at 1 atm is slower than that of melt-bearing olivine at high pressure, Karato’s (1989) “dry” 300 MPa data suggests that grain growth of melt-free olivine at high pressure is faster (Fig. 10). However, from our own experience with San Carlos olivine starting material (Faul et al. 2004) and that of others (Hirth and Kohlstedt 1995), it is difficult to completely eliminate all impurities which produce a melt at high temperature and low pressure (1 atm or 300 MPa). Even with melt pres-

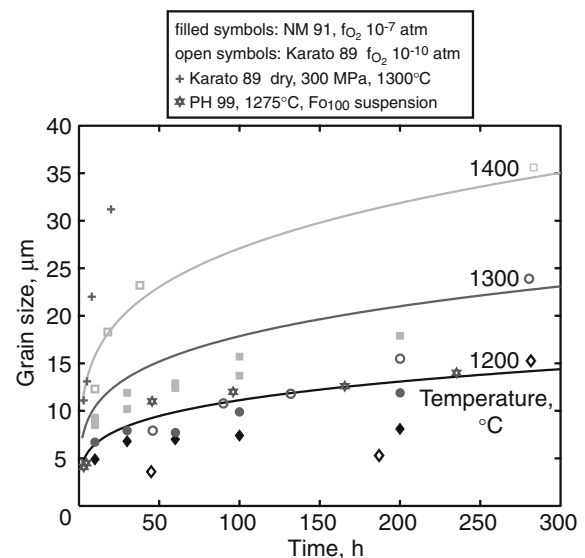


Fig. 10 Comparison of grain growth data for melt-free olivine from the literature with the fit to the data from this study (*solid lines*). Temperature is indicated above the curves by *symbols* for the data of the 1-atm studies (*diamonds* 1,200°C, *circles* 1,300°C, *squares* 1,400°C). *NM 91* Nichols and Mackwell (1991), *Karato 89* Karato (1989) 1 atm and dry 300 MPa data, *PH 99* Park and Hanson (1999). The steeper slopes of Karato’s (1989) data (*open symbols* and *crosses*) corresponds to the smaller exponents ($n=2-3$) relative to the other studies ($n\sim 4$)

ent, however, Karato's grain growth rates are much faster than ours.

A comparison of the growth rates observed in this study and those of Park and Hanson (1999) suggests that growth rates decrease with increasing melt content. This assumes that the differences in composition (Fe-free system in Park and Hanson's (1999) case) and pressure (1 atm vs. 1 GPa) in the two studies do not significantly influence growth rates. Decreasing growth rates with increasing melt contents are observed in a number of liquid phase sintering systems (German and Olevsky 1998). They also point out that solid-state growth is substantially slower than growth at high liquid proportions, requiring a maximum in the growth rate at a critical proportion of liquid, which they infer is near 1%. Their model also assumes that the growth exponent does not change as a function of liquid proportion.

The growth rates observed by Nichols and Mackwell (1991) (melt free), in this study (relatively small amounts of melt) and Park and Hanson (1999) (high melt contents) are consistent with the model proposed by German and Olevsky (1998), although the materials and conditions in these three studies differ somewhat. Despite these differences, the growth exponents as indicated by the slopes of the growth curves in Fig. 10 are similar.

Hirth and Kohlstedt (1995) also determined a rate constant k (Eq. 2) in their experiments at 300 MPa, using the exponent and activation energy determined by Karato (1989). However, their experiments were deformation experiments with excursions into the dislocation creep regime for some samples. Dislocation creep is generally accompanied by grain size reduction due to dynamic recrystallization (Karato 1984). The growth rates observed for their nominally melt-free samples (containing up to 1% melt) are broadly consistent with the growth rates determined in this study.

Experiments with melt-free sol-gel derived olivine (prepared as described above) indicate that grain growth in the absence of melt is very slow: even after > 30 h at 1,200°C and 300 MPa a dry sample only grew to a mean grain size of 3 μm (Jackson et al. 2002). This sample contained minor opx and some pores (observable by TEM imaging but not measurable in the density). The growth rate of this sample is similar to the growth rates determined by Nichols and Mackwell (1991).

Assuming the pores in Nichols and Mackwell's (1991) experiments simply act as a secondary phase reducing growth rates, the kinetics determined from their experiments may be representative for upper mantle rocks, where secondary phases moderate growth rates. Extrapolation of their growth rates and those determined in this study suggests that while partially molten dunite will reach a grain size of 1 mm at 1,400°C in a little more than 50,000 years, sub-solidus grain growth will only reach this grain size in well over 1 Myears (Fig. 11). Evans et al. (2001) similarly concluded that secondary phases moderate grain growth for extrapolated grain sizes to be compatible with grain sizes observed in xenoliths. However, grain growth rates

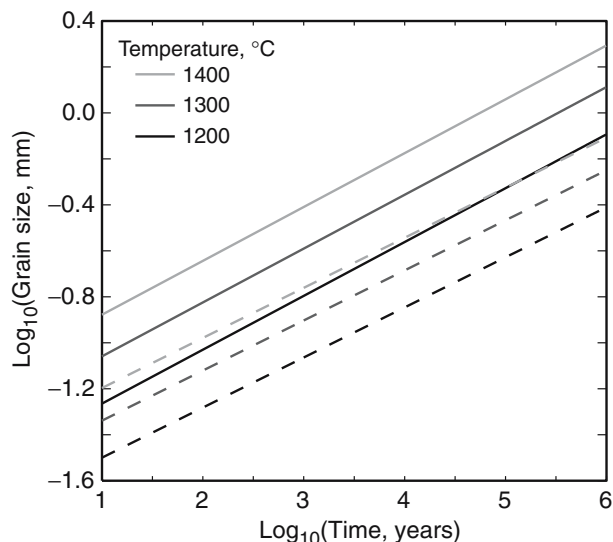


Fig. 11 Extrapolation of growth rates for partially molten dunite from this study (*solid lines*) and growth rates determined by Nichols and Mackwell (1991) for growth controlled by secondary phases (*dashed lines*). For comparison, grain sizes in xenoliths range from a few millimeters to tens of millimeters, see for example Evans et al. (2001) and references therein

significantly increase when water is present (Karato 1989).

Acknowledgements We thank Harri Kokkonen and Bill Hibberson for assistance with various aspects of this study. We also thank Brian Evans and an anonymous reviewer for their constructive comments which significantly improved the manuscript.

References

- Atkinson HV (1988) Theories of normal grain growth in pure single phase systems. *Acta Metall* 36:469–491
- von Bargen N, Waff HS (1986) Permeabilities, interfacial areas and curvatures of partially molten systems: results of numerical computations of equilibrium microstructures. *J Geophys Res* 91:9261–9276
- Bennema P, van der Eerden JP (1987) Crystal graphs, connected nets, roughening transition and the morphology of crystals. Terra Scientific Publishing Co., Tokyo, pp 1–77
- Cabane H, Laporte D, Provost A (2001) Experimental investigation of the kinetics of Ostwald ripening of quartz in silicic melts. *Contrib Mineral Petr* 142:361–373
- Cmíral M, FitzGerald JD, Faul UH, Green DH (1998) A close look at dihedral angles and melt geometry in olivine-basalt aggregates: a TEM study. *Contrib Mineral Petrol* 130:336–345
- Evans B, Renner J, Hirth G (2001) A few remarks on the kinetics of static grain growth in rocks. *Int J Earth Sci* 90:88–103
- Faul UH (1997) Permeability of partially molten upper mantle rocks from experiments and percolation theory. *J Geophys Res* 102:10299–10311
- Faul UH (2001) Melt retention and segregation beneath mid-ocean ridges. *Nature* 410:920–923
- Faul UH, Jackson I (2005) The seismological signature of temperature and grain size variations in the upper mantle. *Earth Planet Sc Lett* 234:119–134
- Faul UH, FitzGerald JD, Jackson I (2004) Shear wave attenuation and dispersion in melt-bearing olivine polycrystals: 2. microstructural interpretation and seismological implications. *J Geophys Res* 109:B06202. DOI 10.1029/2003JB002407

- Fischmeister H, Grimvall G (1975) Ostwald ripening—a survey, vol. 6 of Materials Sciences Research. Plenum Press, pp 119–149
- German RM, Olevsky EA (1998) Modeling grain growth dependence on the liquid content in liquid-phases-sintered materials. *Metall Mater Trans* 29A:3057–3067
- Hanitzsch E, Kahlweit M (1969) Zur Umlösung aufgedampfter Metallkristalle, II. *Z Physik Chemie Neue Folge* 65:290–305
- Hillert M (1965) On the theory of normal and abnormal grain growth. *Acta Metall* 13:227–238
- Hirth G, Kohlstedt DL (1995) Experimental constraints on the dynamics of the partially molten upper mantle: deformation in the diffusion creep regime. *J Geophys Res* 100:1981–2001
- Jackson I, Fitz Gerald J, Faul UH, Tan BH (2002) Grain-size-sensitive seismic wave attenuation in polycrystalline olivine. *J Geophys Res* 107. DOI 10.1029/2001JB001225
- Karato SI (1984) Grain size distribution and rheology of the upper mantle. *Tectonophysics* 104:155–176
- Karato SI (1989) Grain growth kinetics in olivine aggregates. *Tectonophysics* 168:255–273
- Leshar CE, Walker D (1988) Cumulate maturation and melt migration in a temperature gradient. *J Geophys Res* 93:10295–10311
- Lifshitz IM, Slyozov VV (1961) The kinetics of precipitation from supersaturated solid solutions. *J Phys Chem Solids* 19:35–50
- Louat NP (1974) On the theory of normal grain growth. *Acta Metall* 22:721–724
- Martin JW, Doherty RD, Cantor B (1997) Stability of microstructure in metallic systems, 2nd edn. Cambridge University Press, Cambridge, England
- Mulheran PA (1992) The scaling theory of normal grain growth: beyond the mean field approximation. *Phil Mag Lett* 65:141–145
- Nichols SJ, Mackwell SJ (1991) Grain growth in porous olivine aggregates. *Phys Chem Miner* 18:269–278
- Pande CS (1987) On stochastic theories of grain growth. *Acta Metall* 35:2671–2678
- Park Y, Hanson B (1999) Experimental investigation of Ostwald-ripening rates of forsterite in the haplobasaltic system. *J Volcanol Geoth Res* 90:103–113
- Ralph B, Shim KB, Huda Z, Furley J, Edirisinghe MJ (1992) The effects of particles and solutes on grain boundary migration and grain growth. *Mater Sci For* 94–96:129–140
- Renner J, Evans B, Hirth G (2002) Grain growth and inclusion formation in partially molten carbonate rocks. *Contrib Mineral Petr* 142:501–514
- Solomatov VS (2001) Grain size-dependent viscosity convection and the thermal evolution of the Earth. *Earth Planet Sci Lett* 191:203–212
- Taylor WR, Green DH (1989) The role of reduced C-O-H fluids in mantle partial melting. In: Proceedings of the fourth International Kimberlite Conference pp 592–602
- ten Grotenhuis SM, Drury MR, Peach CJ, Spiers CJ (2004) Electrical properties of fine-grained olivine: evidence for grain boundary transport. *J Geophys Res* 109:B06203. DOI 10.1029/2003JB002799
- Tikare V, Cawley JD (1998) Numerical simulation of grain growth in liquid phase sintered materials—II. Study of isotropic grain growth. *Acta Mater* 46:1343–1356
- Ulmer P, Luth RW (1991) The graphite-COH fluid equilibration in P, T, f_{O_2} space: an experimental determination to 30 kb and 1600°C. *Contrib Mineral Petr* 106:265–272
- Waff HS, Faul UH (1992) Effects of crystalline anisotropy on Fluid distributions in ultramafic partial melts. *J Geophys Res* 97:9003–9014
- Wagner C (1961) Theorie der Alterung von Niederschlägen durch Umlösen (Ostwald-Reifung). *Z Elektrochemie* 65:581–591
- Walte ND, Bons PD, Pashier CW, Koehn D (2003) Disequilibrium melt distribution during static recrystallization. *Geology* 31:1009–1012
- Wark DA, Watson EB (1998) Grain scale permeabilities of texturally equilibrated, monomineralic rocks. *Earth Planet Sci Lett* 164:591–605
- Wark DA, Williams CA, Watson EB, Price JD (2003) Reassessment of pore shapes in microstructurally equilibrated rocks, with implications for permeability of the upper mantle. *J Geophysical Res* 108. DOI 10.1029/2001JB001575